

Fourier Collocation Approach With Mesh Refinement Method for Simulating Transit-Time Ultrasonic Flowmeters Under Multiphase Flow Conditions

Matej Simurda , Lars Duggen, Nils T. Basse, and Benny Lassen

Abstract—A numerical model for transit-time ultrasonic flowmeters operating under multiphase flow conditions previously presented by us is extended by mesh refinement and grid point redistribution. The method solves modified first-order stress-velocity equations of elastodynamics with additional terms to account for the effect of the background flow. Spatial derivatives are calculated by a Fourier collocation scheme allowing the use of the fast Fourier transform, while the time integration is realized by the explicit third-order Runge–Kutta finite-difference scheme. The method is compared against analytical solutions and experimental measurements to verify the benefit of using mapped grids. Additionally, a study of clamp-on and in-line ultrasonic flowmeters operating under multiphase flow conditions is carried out.

Index Terms—Fluid flow measurement, numerical simulation, acoustics, propagation, mathematical model, fast Fourier transforms.

I. INTRODUCTION

TRANSIT-TIME ultrasonic flowmeter (TTUF) is a well-matured technology that provides simple, yet accurate measurements of a fluid flow in many industrial areas, such as oil&gas, wastewater treatment, and food industries. The method has been improved on many levels among others' signal processing, transducer design, and temperature compensation [1]. The basic operating principle relies on a reciprocity of the system, which is essential to accurately measure flow velocity. The signals that propagate with and against the flow should be similar in terms of the center frequency and the envelope. This condition is normally well satisfied for flows of homogeneous media, but once the multiphase flow occurs, the signals get distorted. Reciprocity violations then depend on various factors, such as acoustic impedance of the second-phase inclusions, their size versus signal wavelength, and concentration and position of them with respect to the sonic beam. A practical example where TTUF may fail is an oil&gas bubbly flow measurement with high gas void fractions. The

signal can get attenuated so much that very little is received on the other side of the pipe or the scattering from the inclusions modifies the received waveforms, such that upstream and downstream signals are poorly correlated.

Due to the chaotic nature of multiphase flow, it is very difficult to perform measurements with well-controlled distribution of phases, concentrations, and sizes. A statistical approach is another option but performing experiments over a wide range of fluid flow parameters is expensive both in terms of time and economy. A mathematical model that can simulate high volumes of these measurements is an attractive alternative. The simulation results could then be statistically analyzed to check for dependences of the received signal properties on the fluid flow parameters.

Several studies have been previously published on simulations of TTUFs. A semianalytical model presented by Funck and Mitzkus [2] considered a clamp-on measuring setup with transducers shifted from their ideal position where the effect of the misalignment on the flowmeter accuracy was discussed. There have also been numerous numerical approaches published on this problem based on ray-tracing [3]–[6], finite-element methods (FEMs) [3], or combined methods of boundary integral method and FEM [7]. All methods showed good results but have weaknesses. The most flexible methods require a high number of points per minimum wavelength (PPMW), thus being computationally expensive. The less computationally expensive methods, however, are typically not capable of solving for arbitrary flow profiles or multiphase flow cases. The most recent contribution was done by Luca *et al.* [8]–[10] who presented a numerical model of TTUF based on the discontinuous Galerkin method, which is computationally efficient and allows to solve for complex flow patterns. Spectral methods are a family of numerical methods for partial differential equations, which came into their own in 1970s [11] but still lack broad commercial distribution. Some exceptions can be found in MATLAB open-source toolboxes [12] that, however, are clearly not as widespread as the classical engineering alternatives, such as finite-difference (FD) methods (Wave2000 and Wave3000 [13]) and FEM (COMSOL [14] and ANSYS [15]). Their potential of using them for simulating wave propagation lies in the fact that they seek the solution as a sum of shape functions that are nonzero over the entire domain. Selecting these functions in a smart way allows to describe the wave propagation accurately enough but with fewer PPMW compared with FEM or FD

Manuscript received October 3, 2017; accepted November 10, 2017. Date of publication November 20, 2017; date of current version January 26, 2018. (Corresponding author: Matej Simurda.)

M. Simurda was with the Mads Clausen Institute, University of Southern Denmark, 6400 Sønderborg, Denmark. He is now with Orsted, 7000 Fredericia, Denmark (e-mail: simurda@mci.sdu.dk).

L. Duggen is with the Mads Clausen Institute, University of Southern Denmark, 6400 Sønderborg, Denmark (e-mail: duggen@mci.sdu.dk).

N. T. Basse was with Siemens A/S Flow Instruments, 6400 Sønderborg, Denmark. He is now with Danfoss A/S, Refrigeration and Air Conditioning Controls, 6430 Nordborg, Denmark.

B. Lassen is with Orsted, 7000 Fredericia, Denmark.

Digital Object Identifier 10.1109/TUFFC.2017.2775283

methods, hence decreasing computation power demands. The global nature of these methods, however, causes some issues when solving problems, including parameter discontinuities, since the local mesh refinement is less trivial than with the local approaches. An example of a pseudospectral method mapped on a 1-D nonuniform grid can be found in [16]. Alternatively, the immersed boundary method can be employed to resolve complicated geometrical features [17], [18].

In this paper, a pseudospectral Fourier collocation method for solving elastic and acoustic wave propagation in ultrasonic flowmeters is presented. Spatial derivatives are calculated by the Fourier collocation method, and the time integration is realized by the FD scheme. Although this method has been previously described and tested [19], [20], a regular uniform grid has always been used as the computational domain. This poses difficulties to accurately resolve any parameter discontinuities or complex geometrical shapes. In this paper, special attention is dedicated to grid mapping and 1-D mesh refinement in order to accurately solve the scattering from second-phase inclusions and transmission through pipe walls, respectively. The effect of the mesh refinement on the simulation accuracy is discussed by comparing to analytical solutions and experimental measurements. Finally, models of clamp-on and in-line TTUFs together with a study of effect of multiphase flow on the measurement accuracy are presented.

II. GOVERNING EQUATIONS

A linear propagation of acoustic waves in homogeneous isotropic media can be described by the equations of linear elasticity [21]

$$\frac{\partial \sigma_{ij}}{\partial t} = \lambda \delta_{ij} \frac{\partial v_l}{\partial x_l} + \mu \left(\frac{\partial v_i}{\partial x_j} + \frac{\partial v_j}{\partial x_i} \right) \quad (1)$$

$$\rho \frac{\partial v_i}{\partial t} = \frac{\partial \sigma_{ij}}{\partial x_j} + f_i \quad (2)$$

where σ_{ij} , v_i , λ , μ , and f_i are the stress, displacement velocity, Lamé first parameter, shear modulus, and body force, respectively. The *Einstein* summation convention is used, and δ_{ij} denotes the *Kronecker* delta. Propagation in acoustic media can be modeled by setting shear modulus to zero. The longitudinal c_p and shear c_s wave speeds in infinite homogeneous media are related by the material parameters as

$$c_p = \sqrt{\frac{\lambda + 2\mu}{\rho}}, \quad c_s = \sqrt{\frac{\mu}{\rho}}. \quad (3)$$

Equations (1) and (2) are valid for quiescent media. The effect of the background flow can be modeled by including extra terms [22]

$$\begin{aligned} \frac{\partial \sigma_{ij}}{\partial t} &= \lambda \delta_{ij} \frac{\partial v_l}{\partial x_l} + \mu \left(\frac{\partial v_i}{\partial x_j} + \frac{\partial v_j}{\partial x_i} \right) \\ &\quad - \delta_{ij} v_{0l} \frac{\partial \sigma_{ij}}{\partial x_l} - \delta_{ij} \sigma_{ij} \frac{\partial v_{0l}}{\partial x_l} \end{aligned} \quad (4)$$

$$\rho \frac{\partial v_i}{\partial t} = \frac{\partial \sigma_{ij}}{\partial x_j} + f_i - \rho v_{0l} \frac{\partial v_i}{\partial x_l} - \rho v_l \frac{\partial v_{0i}}{\partial x_l} \quad (5)$$

where v_{0l} is the background flow allowed to be nonzero only in acoustic media.

III. NUMERICAL METHOD

In this paper, a pseudospectral time domain (PSTD) method is used to discretize and solve (4) and (5) in two spatial dimensions. The method combines the Fourier collocation method to evaluate spatial derivatives and the FD method to integrate with respect to time.

A. Fourier Collocation Method

The Fourier collocation method interpolates the solution in a basis of trigonometric functions and evaluates the derivative in the Fourier space. For an arbitrary interval of length l discretized into N evenly distributed points with step size Δx ($l = \Delta x N$), the derivative can be approximated by [23]

$$\frac{\partial[\cdot]}{\partial x} \approx \text{Re}(\mathcal{F}^{-1}(ik\mathcal{F}(\cdot))) \quad (6)$$

where \mathcal{F} and \mathcal{F}^{-1} are the discrete *Fourier* and inverse *Fourier* transforms of a function $f(x)$, respectively

$$\begin{aligned} \mathcal{F}(f(x))(k) &= \hat{f}(k) = \Delta x \sum_{j=1}^N f(x_j) e^{-ikx_j} \\ \mathcal{F}^{-1}(\hat{f}(k))(x) &= f(x) = \frac{1}{\Delta x N} \sum_{j=1}^N \hat{f}(k_j) e^{ik_j x} \end{aligned} \quad (7)$$

and k is the vector of wavenumbers

$$k = \begin{cases} \left[-\frac{N}{2}, -\frac{N}{2} + 1, \dots, \frac{N}{2} - 1 \right] \frac{2\pi}{\Delta x N}, & \text{if } N \text{ is even} \\ \left[-\frac{N-1}{2}, -\frac{N-1}{2} + 1, \dots, \frac{N-1}{2} - 1 \right] \frac{2\pi}{\Delta x N}, & \text{if } N \text{ is odd.} \end{cases}$$

Such a representation can be implemented very efficiently on a computer as the k vector is calculated and stored upfront, and the FFT algorithm is employed to perform discrete *Fourier* and inverse *Fourier* transforms.

In this paper, we consider fluid mixtures of very high acoustic impedance mismatch for which the Fourier collocation method would inherently develop numerical issues due to the *Gibbs* phenomenon. An alternative approach is to define the entire flowing fluid as a homogeneous medium with the properties of the host medium and manually impose zero values on the stress variables at grid points of second-phase inclusions at each time integration stage. This results in total reflection on the phase boundaries, which is an acceptable approximation for the mixtures within the scope of this paper. That way, we also mitigate numerical issues that would be associated with spectral differentiations of mass density [19], [20].

B. Finite-Difference Method

The third-order *Runge-Kutta* (RK3) method with the *Butcher* tableau presented in Table I was implemented to evaluate time derivatives.

TABLE I
BUTCHER TABLEAU FOR THE RK3 METHOD

0			
1/2	1/2		
3/4	0	3/4	
	2/9	1/3	4/9

Considering a quiescent medium ($v_{0l} = 0$) and following the rule of thumb [23] that the eigenvalues of the problem:

$$\frac{d\hat{u}}{dt} = A\hat{u}, \quad \hat{u} = \begin{bmatrix} \mathcal{F}(\sigma) \\ \mathcal{F}(u) \end{bmatrix} \quad (8)$$

should lie in the stability region, the time stepping restriction is

$$CFL < \frac{1.73}{\pi} \quad (9)$$

where CFL is the Courant–Friedrichs–Lewy number defined as

$$CFL = \frac{\max(c)\Delta x}{\Delta t} \quad (10)$$

where $\max(c)$ ensures that the sound speed c of the fastest medium in the computational domain is always used. In this paper, we consider industrial applications within the subsonic region ($(v_{0l}/c_p) \ll 1$). In such a case, presence of the additional background flow terms in (4) and (5) introduces a real part to the eigenvalues which is, however, of several orders of magnitude smaller than the imaginary part. The flow terms can be therefore thought of as a perturbation to the case of quiescent fluid and will not change the stability picture unless simulating for very long times. The same criterion (9) is therefore used in the following discussions.

C. Staggered Grids

Efficiency and stability of the method can be improved by evaluating stress and kinematic unknowns on grids that are shifted by half of the discretization step $\Delta x_i/2$. Special care needs to be taken to compensate for the shift when evaluating the spatial derivatives so the differential operators are modified appropriately

$$\frac{\partial[\cdot]}{\partial x^\pm} \approx \text{Re}(\mathcal{F}^{-1}(ike^{\pm ik\Delta x/2}\mathcal{F}(\cdot))) \quad (11)$$

where \pm denotes the spatial staggering in the positive and the negative direction, respectively. Additionally, the material properties need to be interpolated at the staggered points to ensure consistency between the computational domains.

It should be noted that staggering with respect to time is often implemented as well [12], [24]–[26]. This technique, however, is impossible in our case due to the presence of the background flow terms v_{0l} that yields (4) and (5) not interlaced [27].

D. Perfectly Matched Layers

One is usually interested only in a very short section of a pipeline when simulating acoustic wave propagation in the TTUF. This transfers to the modeling requirement of imposing

boundary conditions that allow for acoustic waves to propagate out of the simulation domain without inducing any reflections at the boundary. Since the Fourier collocation method inherently imposes periodic boundary conditions, waves leaving the domain on one side will instantly enter on the opposite one, sometimes referred to as *wave wrapping* [24]. In order to eliminate this effect, multi-axial perfectly matched layers (PMLs) [28] are used to truncate the computational domain.

The governing equations (4) and (5) are modified by introducing an additional parameter G_m and artificial splitting of the acoustic field into components associated only with spatial derivatives with respect to one coordinate [19]

$$\begin{aligned} \frac{\partial_m \sigma_{ij}}{\partial t} &= \lambda \delta_{ij} \frac{\partial v_m}{\partial x_m} + \mu \left(\delta_{mj} \frac{\partial v_i}{\partial x_j} + \delta_{mi} \frac{\partial v_j}{\partial x_i} \right) \\ &\quad - \delta_{ij} v_{0m} \frac{\partial \sigma_{ij}}{\partial x_m} - \delta_{ij} \sigma_{ij} \frac{\partial v_{0m}}{\partial x_m} \\ &\quad - m \sigma_{ij} G_m, \end{aligned} \quad (12)$$

$$\begin{aligned} \frac{\partial_m v_i}{\partial t} &= \frac{1}{\rho} \frac{\partial \sigma_{im}}{\partial x_m} + \frac{1}{2\rho} f_i - v_{0m} \frac{\partial v_i}{\partial x_m} \\ &\quad - v_m \frac{\partial v_{0i}}{\partial x_m} - m v_i G_m \end{aligned} \quad (13)$$

$$\sigma_{ij} = \sum_m m \sigma_{ij} \quad (14)$$

$$v_i = \sum_m m v_i \quad (15)$$

where $l, m, n = x, y, z$. Note that the summation convention is not used in (12) and (13). The PML damping parameter G_m is, in this paper, defined as

$$\begin{aligned} G_m &= A_{\text{PML}}(x_l - x_{l0})^{n_{\text{PML}}} \\ &\quad + A_{\text{PML}} r_{\text{PML}} (1 - \delta_{lm})(x_m - x_{m0})^n \end{aligned} \quad (16)$$

where x_{l0} is the coordinate at the inner edge of the PML. The specific values of magnitude A_{PML} , order n_{PML} , ratio r_{PML} , and width of the PML d_{PML} are chosen experimentally so the wave amplitudes at the periodic boundaries get attenuated to the order of computational precision, but the reflections at the interfaces are of negligible magnitudes. Following [29], one can exploit the fact that the governing equations are in the form of $\partial R/\partial t = GR + Q$ and rearrange them in the equivalent representation as $\partial(e^{Gt}R)/\partial t = e^{Gt}Q$, which is a more stable form for numerical implementation as G_m values typically grow to magnitudes several orders higher than unknown kinematic and stress variables.

IV. MESH ADAPTATION

Simulating TTUFs is associated with the presence of discontinuities in parameters λ , μ , and ρ at the location of interfaces between different materials. Moreover, once simulating for a multiphase flow, additional interfaces will also appear in the flowing fluid. These interfaces between the two phases are often of irregular shape that might not be accurately described by the regular uniform grid associated with the PSTD method. One should therefore come up with a mapping between the uniform grid x_u and the nonuniform grid x_n , where discontinuities or sharp parameter features are resolved on a finer

scale and geometrical shapes described more accurately [16]. Using the chain rule, such mapping will modify the spatial derivatives as

$$\frac{\partial[\cdot]}{\partial x_n} = \frac{dx_u}{dx_n} \frac{\partial[\cdot]}{\partial x_u} \approx \frac{dx_u}{dx_n} \text{Re}(\mathcal{F}^{-1}(ik_x \mathcal{F}(\cdot))). \quad (17)$$

In this section, the two approaches for mesh adaptation that were used in this paper are described. The two different approaches are taken because of the nature of the problem we want to solve: transmission through the pipe wall and scattering from bubbles. Some steps of the below described approaches involve finding an inverse of a function. This is done numerically in this paper, since finding the inverse analytically appears to be nontrivial. The same procedure when constructing the grid mappings is followed when using staggered grids. One should always take special care when mapping the nonuniform grid as $x_n(x_u + \Delta x/2)$ and evaluate (dx_u/dx_n) at these points, since the uniform staggering $\Delta x/2$ on the uniform grid is mapped as a nonuniform staggering in the x_n domain.

A. Mesh Refinement

The transmission through the pipe wall can be improved by adding extra points locally at the interface. For convenience, we describe the method in one dimension only. Consider an interval $[x_{\min}, x_{\max}]$ with M number of interfaces located at x_i and a desired uniform spatial discretization step size Δx everywhere besides a close vicinity to the interfaces. The mesh refinement is constructed in the following steps.

- 1) Define the unscaled mapping \tilde{x}_u as

$$\tilde{x}_u = x_n + \sum_{i=1}^M a_i \tanh(b_i(x_n - x_i)). \quad (18)$$

- 2) Rescale the mapping back to the original interval so that $x_u(x_{\min}) = x_{\min}$ and $x_u(x_{\max}) = x_{\max}$

$$\begin{aligned} x_u &= a_{\text{scale}} \tilde{x}_u + b_{\text{scale}} \\ a_{\text{scale}} &= \frac{(x_{\max} - x_{\min})}{\tilde{x}_u(x_{\max}) - \tilde{x}_u(x_{\min})} \\ b_{\text{scale}} &= (x_{\max} + x_{\min}) - a_{\text{scale}} \frac{(x_{\max} + x_{\min})}{2}. \end{aligned} \quad (19)$$

- 3) Define a uniform grid \mathbf{x}_{nmap} with a significantly finer step size Δx_{map} compared with Δx and generate $\mathbf{x}_{\text{umap}}(\mathbf{x}_{\text{nmap}})$ as a numerical representation of the mapping (19).
- 4) Define a uniform grid \mathbf{x}_u as

$$\begin{aligned} \mathbf{x}_u &= [x_{\min}, x_{\min} + a_{\text{scale}} \Delta x, \dots \\ &\dots, x_{\min} + N a_{\text{scale}} \Delta x], \quad N = \left\lceil \frac{x_{\max} - x_{\min}}{a_{\text{scale}} \Delta x} \right\rceil \end{aligned} \quad (20)$$

where $\lceil \cdot \rceil$ denotes rounding up to the closest integer.

- 5) Construct numerically the nonuniform grid \mathbf{x}_n by linearly interpolating $\mathbf{x}_{\text{nmap}}(\mathbf{x}_{\text{umap}})$ and evaluating at \mathbf{x}_u .

- 6) Calculate $(dx_u/dx_n)(\mathbf{x}_n)$ using

$$\frac{dx_u}{dx_n} = a_{\text{scale}} \left(1 + \sum_{i=1}^M a_i b_i (1 - \tanh^2(b_i(x_n - x_i))) \right). \quad (21)$$

The constants a_i and b_i in (18) associated with \tanh are adjustable parameters and can be chosen separately for each interface depending on specific material properties and the respective acoustic impedance mismatch. The computational grid is slightly extended in step 4 because of the rounding up of N to the closest integer. This, however, should not affect the simulation results as the domain is truncated by PMLs anyway.

B. Mesh Stretching

The above-described method is suitable for cases where transmission has to be solved as well. Using this method in two or more spatial dimensions would, however, lead to adding extra points globally along the entire domain as the local mesh refinement is not quite possible with the above-described PSTD method. On the other hand, as, in this paper, we only consider scattering from high acoustic contrast agents, we can stretch the points that are associated with the inside of the bubble toward the interface as we do not solve for the propagation inside the bubble anyway (see Section III-A). Given a uniform grid $\mathbf{x}_u, \mathbf{y}_u$ with step size $\Delta x, \Delta y$ on the interval $[x_{\min}, x_{\max}] \times [y_{\min}, y_{\max}]$. The idea of the proposed stretching algorithm for a circular inclusion of radius R placed in the center of origin can be described in the following steps.

- 1) Consider 1-D uniform grid \mathbf{r}_{umap} on the interval $[-n_R R, n_R R]$ with a significantly finer step size Δr_{map} compared with Δx and Δy .

- 2) Predefine coordinate mapping as

$$\tilde{\mathbf{r}}_{\text{nmap}} = \mathbf{r}_{\text{umap}}. \quad (22)$$

- 3) Identify all the grid points satisfying

$$\mathbf{r}_{\text{umap}}^2 \leq R^2. \quad (23)$$

- 4) Remap each such grid point as

$$\tilde{\mathbf{r}}_{\text{nmap}} = \mathbf{r}_{\text{umap}} + \mathbf{d} \quad (24)$$

$$\mathbf{d} = \Delta \mathbf{r} - \frac{\Delta \mathbf{r}^2}{R} \quad (25)$$

$$\Delta \mathbf{r} = R - |\mathbf{r}_{\text{umap}}|. \quad (26)$$

- 5) Smooth the final mask by numerical convolution with normalized Gaussian

$$\mathbf{r}_{\text{nmap}} = \tilde{\mathbf{r}}_{\text{nmap}} * \mathbf{g}(\mathbf{r}_{\text{umap}}) \quad (27)$$

$$\mathbf{g} = \frac{e^{-\frac{\mathbf{r}_{\text{umap}}^2}{2\sigma^2}}}{\sigma^2 2\pi} \quad (28)$$

$$\sigma = a_\sigma R \quad (29)$$

where a_σ is an adjustable parameter that determines the smoothing strength of the convolution. The specific value of n_R is chosen based on a_σ , such that the edges of the mapping transition back to the uniform grid.

- 6) Calculate $(dr_u/dr_n)(\mathbf{r}_{\text{nmap}})$ numerically using an FD scheme.
- 7) Construct numerically the nonuniform grid \mathbf{r}_n by linearly interpolating $\mathbf{r}_{\text{nmap}}(\mathbf{r}_{\text{umap}})$ and evaluating at $\mathbf{r}_u = (\mathbf{x}_u^2 + \mathbf{y}_u^2)^{1/2}$.
- 8) Calculate \mathbf{x}_n and \mathbf{y}_n using a simple polar coordinate transform

$$\mathbf{x}_n = \mathbf{x}_n \cos \phi \quad (30)$$

$$\mathbf{y}_n = \mathbf{y}_n \sin \phi \quad (31)$$

$$\phi = \arctan \frac{\mathbf{x}_u}{\mathbf{y}_u} \quad (32)$$

and likewise all the mapping gradients.

The same technique can be applied to an arbitrary cylindrical inclusion positioned at $[x_R, y_R]$ with a simple coordinate transform

$$\tilde{\mathbf{x}}_{\text{umap}} = \mathbf{x}_{\text{umap}} - x_R, \quad \tilde{\mathbf{y}}_{\text{umap}} = \mathbf{y}_{\text{umap}} - y_R. \quad (33)$$

V. TEST CASES

In this section, several test cases to verify the method are presented. The original method that uses uniform grid has been previously validated against analytical solutions, and issues, such as dispersion errors, have been discussed as well [19]. The following test cases are therefore focused on the grid adaptation techniques.

A. Transmission and Reflection: Normal Incidence

A first example demonstrates the benefit of using mesh refinement described in Section IV-A. Consider a normal incidence of a plane wave on an interface between two homogeneous media. It is sufficient to model such a scenario in 1-D to examine the mesh refinement effect.

A point source is located at x_s in the first material (λ_1 and ρ_1). The interface is located at x_i and one receiver is positioned at x_{rr} in the second material (λ_2 and ρ_2) and one at x_{rt} in the first material to record reflected and transmitted waves, respectively. The input signal is a single sine wave pulse of a frequency f_c multiplied by the Hanning window. All parameters are tabulated in Table II. A series of simulations was performed for varying PPMW values for both uniform and refined grid, and the results were subsequently compared with an analytical solution. The time step Δt in all studies presented here is determined via the Courant–Friedrichs–Lewy number $CFL = (\max(c_p) \min(\Delta x_n, \Delta y_n) / \Delta t)$. It is sufficient to check only for maximal longitudinal speed as $c_p > c_s$ for isotropic materials assumed in this paper.

Examples of simulated received signals are presented in Fig. 1 where an improvement is observed especially for the reflected waves. The signal calculated on the nonuniform mesh is closer to the analytical solution in both shape and magnitude. The simulated transmitted waves are quite accurate for both grids although some improvement in magnitude is still observed especially for the cases of low PPMW value.

The errors of the simulated signals are quantified in Fig. 2 as a function of PPMW. The overall benefit of using refined

TABLE II
PARAMETERS OF THE 1-D INCIDENCE ON THE INTERFACE
BETWEEN TWO HOMOGENEOUS MEDIA

f_c	1	MHz
d	14	mm
x_{rr}	-7	mm
x_{rt}	7	mm
ρ_{host}	1024.4	kg/m ³
λ_{host}	2.25	GPa
CFL	0.2	-
a_i	10^{-3}	-
b_i	2100	-

meshes is obvious and appears to be necessary when simulating clamp-on TTUFs where transmission and reflection on interfaces of two homogeneous media occur frequently.

B. Point Source in a Homogeneous Medium With a Cylindrical Inclusion

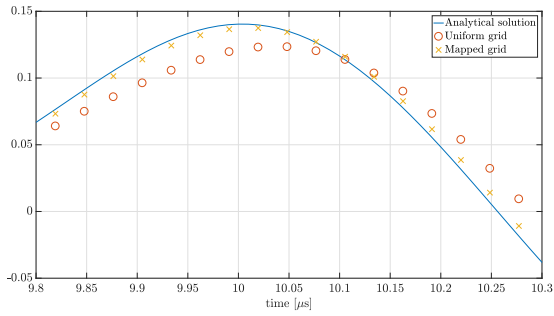
In this example, a scattering of compressional waves propagating in a homogeneous host medium ($\lambda_{\text{host}}, \rho_{\text{host}}$) from a circular inclusion ($\lambda_{\text{inclusion}}, \rho_{\text{inclusion}}$) of radius a positioned at the center of coordinate system is modeled. The measurement setup is schematically depicted in Fig. 3. A point source is located at $x_s = -d$ and $y_s = 0$ and the receiver at $x_r = d$ and $y_r = 0$. All parameters are tabulated in Table III. The host medium is water, and the circular inclusion is assumed to be an air bubble. Considering the high acoustic impedance mismatch, the alternative approach of manually assigning zero stress values at the grid points associated with the cavity (described in Section III-A) was taken instead. The input signal is a burst of N sine pulses of frequency f_c multiplied by the Hanning window. A series of simulations was again performed for varying PPMW values and ratio of the inclusion diameter $D = 2a$ to the signal wavelength $\lambda_s = (c_p/f_c)$ (DPW) for both uniform and refined grids. Simulating wave propagation over distances of tenths of wavelengths revealed numerical instabilities always first appearing at the interface of the cylindrical inclusion. A filter in Fourier space of the form

$$w = (1 - \sin^{22}(k_x \Delta x/2)) \cdot (1 - \sin^{22}(k_y \Delta y/2)) \quad (34)$$

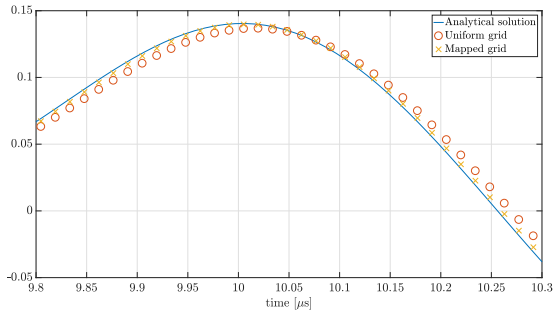
was therefore used at each time integration step to stabilize the method, where Δx and Δy are the spatial steps far from the cylindrical inclusion where mesh is uniform. The filter will artificially dampen the solution, but only about 30% of the highest supported frequencies are effected so using $\text{PPMW} \geq 4$ should not affect the simulation results significantly.

The simulation results from the pseudospectral model were subsequently compared with finite-element models built in COMSOL [14] for the same parameters. A mesh convergence study was conducted for these models to ensure that any numerical errors caused by the spatial discretization are negligible.

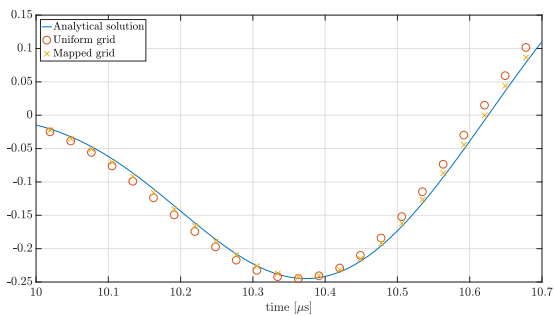
Fig. 4 represents a comparison of the normalized L_2 errors as a function of PPMW and DPW for the regular grid and the mapped grid described in Section IV-B. The value of



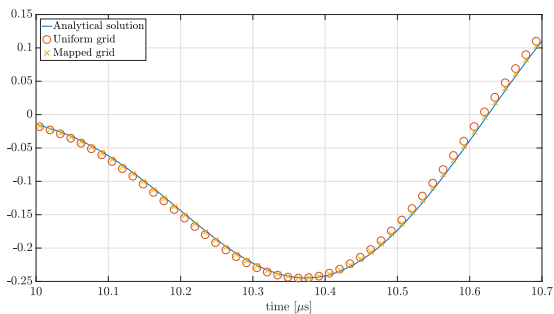
(a)



(b)



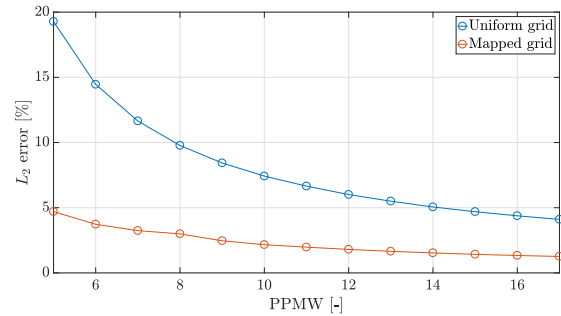
(c)



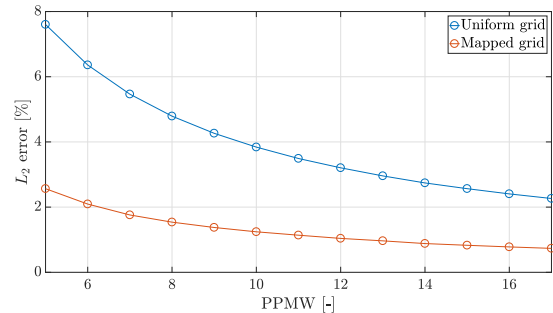
(d)

Fig. 1. Comparison of the simulated received signals for uniform and mapped grid together with the analytical solution for 1-D incidence on the interface between two homogeneous media. (a) Received reflected signal $PPMW = 5$. (b) Received reflected signal $PPMW = 10$. (c) Received transmitted signal $PPMW = 5$. (d) Received transmitted signal $PPMW = 10$.

PPMW for the nonuniform grid cases is assumed to be evaluated far from the inclusion where the grid is regular. The normalized errors consistently decrease with increasing PPMW and are generally lower when the mapped grid is



(a)



(b)

Fig. 2. L_2 errors of simulated transmitted and reflected waves for uniform and mapped grid. (a) Reflected signal. (b) Transmitted signal.

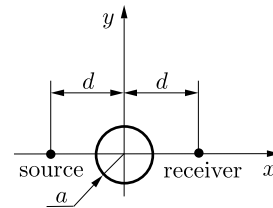


Fig. 3. Cylindrical inclusion setup scheme [20].

TABLE III
PARAMETERS OF THE MODEL OF POINT SOURCE IN A HOMOGENEOUS MEDIUM WITH A CYLINDRICAL INCLUSION

f_c	1	MHz
d	14	mm
ρ_{host}	1024.4	kg/m ³
λ_{host}	2.25	GPa
$\rho_{\text{inclusion}}$	1.2	kg/m ³
$\lambda_{\text{inclusion}}$	0.14	GPa
CFL	0.05	-
$PPMW$	5, 6, ..., 17	-
DPW	0.25, 1, 3, 4	-
n_R	0.05	-

employed. In contrast, the uniform grid sometimes yields higher error for increased PPMW. This can be explained by the rasterization of the circular inclusion on the regular grid, where the effective area of the inclusion is not necessarily preserved. There is one exception where the uniform grid yields more accurate result, particularly $DPW = 0.25$ and $PPMW = 5$. The grids are too coarse to capture the inclusion in such case. Nevertheless, the grid adaptation algorithm is still employed

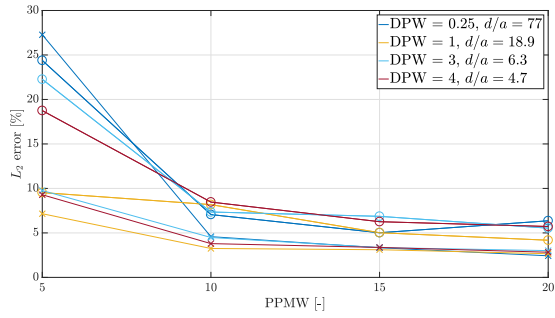


Fig. 4. L_2 errors of uniform (○) and mapped (×) grid for the cylindrical inclusion setup.

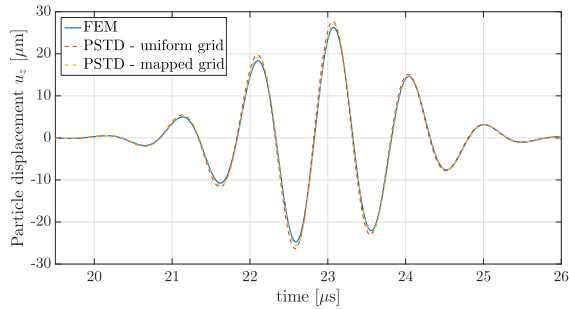


Fig. 5. Received signals for the cylindrical inclusion setup PPMW = 10 and DPW = 1.

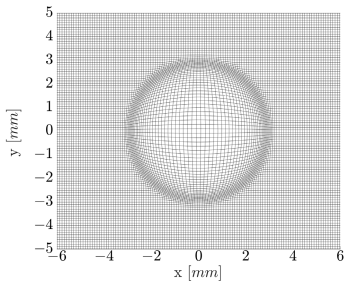


Fig. 6. Example of a nonuniform grid for a circular inclusion of diameter $D = 3$ mm.

for the nonuniform grid. This generates discontinuities in (dx_u/dx_n) terms and in turn produces higher numerical errors than for the regular grid. The overall benefit of using the optimized grids over the regular ones is, however, still evident. It has been verified that using L_∞ norm leads to similar conclusions and its comparison is therefore omitted from this discussion. An example of received signals is presented in Fig. 5. An example of the mapped grid for a single circular inclusion of diameter $D = 3$ mm is depicted in Fig. 6.

C. Experimental Measurements

A simple measurement setup similar to the test case presented in Section V-B was used to verify the model experimentally [20]. Two ultrasonic transducers with piezoceramic crystal of center frequency f_c matched to a half-wavelength steel window were immersed each on one side of a waterbath separated by distance d . Cylinders of different radii a were used as air phantoms. They were manufactured from thin

TABLE IV
PARAMETERS OF THE MODEL AND THE EXPERIMENTAL MEASUREMENT SETUP

d	39.4	mm
l	138.7	mm
w	16.1	mm
a	2.05, 3, 4	mm
λ_{water}	2.25×10^9	Pa
ρ_{water}	1024.4	kg/m ³
$\Delta x = \Delta y$	0.13	mm
CFL	0.2	-
n_R	0.05	-
V_{pp}	10	V
f_c	1	MHz

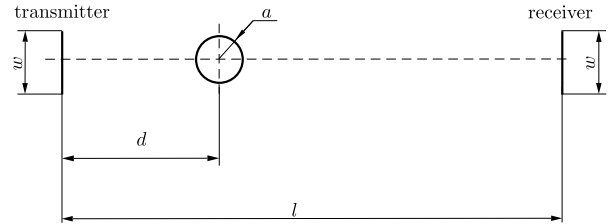


Fig. 7. Experimental measurement setup scheme [20].

aluminum foil, which do not need to be included in the model as its thickness is declared to be about 75 times smaller than the expected wavelength of 1-MHz signal in water.

The measurement setup, identical to the one used in the previous study [20], is schematically depicted in Fig. 7 together with parameters tabulated in Table IV. A voltage signal burst of five sine cycles with peak-to-peak voltage V_{pp} was generated by the Agilent 33120A Waveform Generator, and the received voltage was measured over a serial 50- Ω resistor in the receiver circuit. Waveforms shown in Fig. 8 were captured using the Agilent MSO6014A digital oscilloscope. The 1-D transducer model developed by Willatzen [30], [31] was used to transfer from electric signal to stress-velocity variables and back.

Properties of the piezoceramic material were found by optimizing the error between the measurement and the simulation results for the case of propagation in a homogeneous medium. Curves depicted in Fig. 8(a) are, therefore, in a very good agreement. The remaining comparisons exhibit some differences in both magnitude and envelope shape. It has been previously argued [20] that the magnitude differences were partially caused by the rasterization of the circular phantoms on a regular grid. It is, however, observed that the signals from the nonuniform grid simulations are of the similar shape and magnitude. This is very likely due to the fact that the phantoms are of quite large diameter compared with the wavelength of the 1-MHz acoustic signal in water and the curvature of the inclusion is therefore sufficiently described even on the uniform grid. The source for both types of discrepancies therefore likely lies in the inaccurate model of the transducer that assumes the crystal to operate in a thickness mode. Placement of inclusion in the sonic path results in nonuniform pressure on the receiver plane. This excites transverse waves

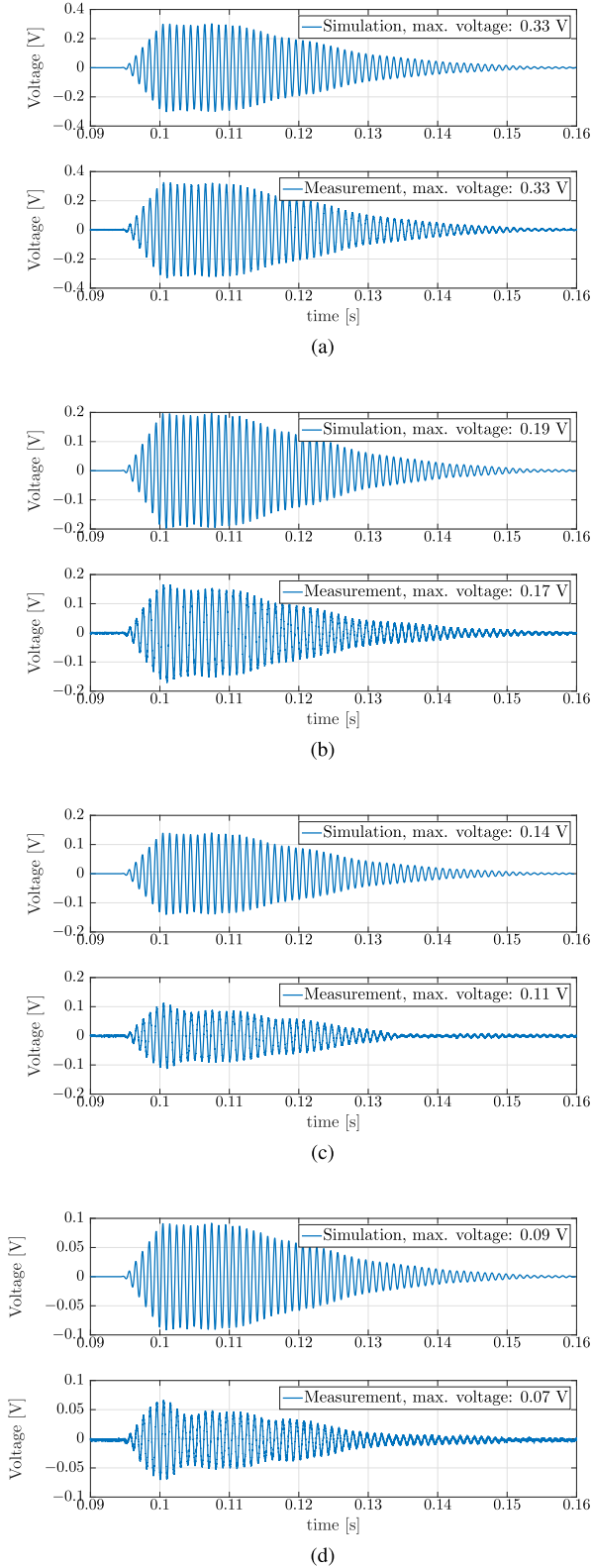


Fig. 8. Comparison of the experimental measurements and the simulation results. (a) Case I: homogeneous medium. (b) Case II: $d = 4.1$ mm. (c) Case III: $d = 6$ mm. (d) Case III: $d = 8$ mm.

in the steel window and possibly other than thickness mode vibrations in the piezocrystal. Such complex vibrations result in a different envelope of the received signal, and at the same time, less voltage is generated in the receiver circuit.

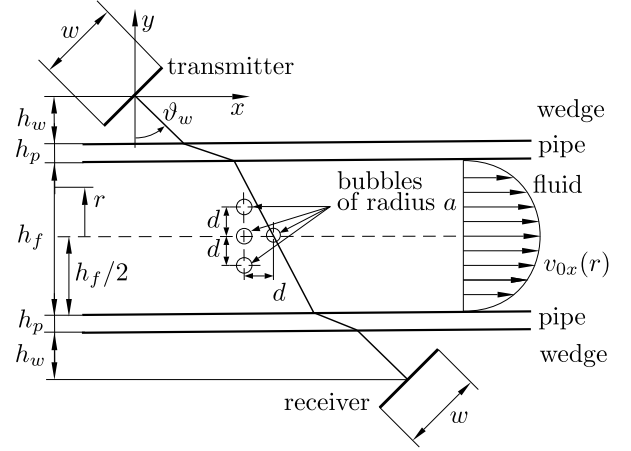


Fig. 9. Clamp-on flowmeter scheme [20].

VI. FLOWMETER SIMULATIONS

In this section, a model of clamp-on and in-line TTUF is presented, and scenarios of these devices operating under homogeneous and multiphase flow conditions are discussed with respect to the measurement accuracy. In both the cases, an excitation from the transducer is modeled as a P-wave line source [24], where the input signal is again a train of sine pulses multiplied by the *Hanning* window. The received signal is calculated by averaging the values of the normal stress σ_n on the receiver line. The simulated measurement error is calculated by running a simulation of the transmit signal propagating upstream and downstream, respectively. The standard flow equation is then used [2]

$$\bar{v} = k_h \frac{c_0}{\sin \vartheta_0} \frac{\Delta t}{2t_{f0}} \quad (35)$$

where t_{f0} is the transit time in quiescent fluid, c_0 is the primary wave sound velocity, and ϑ_0 is the angle of the ultrasonic beam in the transducer medium with respect to pipe axis. A longitudinal cross section of the center of the pipe for clamp-on measurement setup ($c_0 = c_w$ and $\vartheta_0 = \vartheta_w$) is schematically depicted in Fig. 9 together with all geometrical parameters. The same equation can be used for the in-line TTUF with the difference that c_0 and ϑ_0 are the parameters related to the flowing fluid ($c_0 = c_f$ and $\vartheta_0 = \vartheta_f$). Δt is the difference of transit times that is calculated by cross correlating the upstream and downstream received signals and the correlation peak is interpolated by a third-order polynomial fit on the four points of a maximum correlation value. The flow equation is usually derived under the assumption of signal propagating in form of plane waves and a uniform flow profile across the pipe. While the first is usually well satisfied for cases of homogeneous flow, the latter deviates from the experience of practical applications. The difference of transit times Δt measured by TTUFs is averaged over the acoustic path from the transducer to the receiver, and a so-called hydraulic factor k_h is introduced in the flow equation to compensate for the varying flow velocity across the pipe. In this paper, the focus is on the effect of the multiphase flow on the flowmeter accuracy and not the flow profile. A power-law flow profile $v_{x0}(r)$ is,

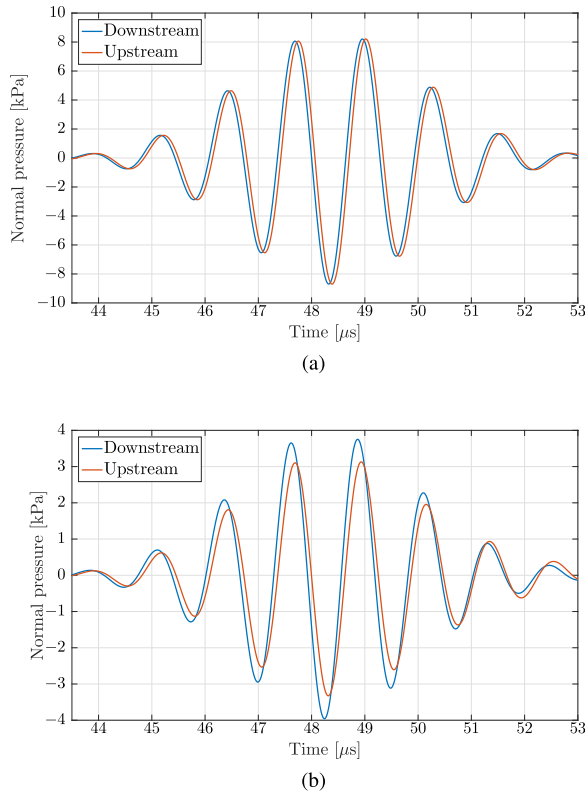


Fig. 12. Comparison of the simulated received signals for homogeneous and multiphase flow for in-line TTUF, $v_{0x} = 5 \text{ m}\cdot\text{s}^{-1}$. (a) Homogeneous flow. (b) Multiphase flow.

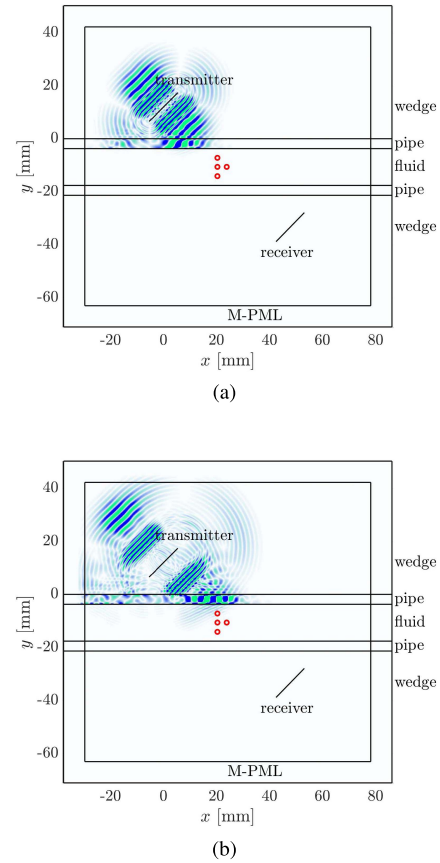


Fig. 15. Simulation snapshots for the clamp-on flowmeter showing normal stress σ_{xx} . No scale is shown as the color map is intentionally saturated to clearly visualize the pressure fields in the different media. (a) Time $t = 10 \mu\text{s}$. (b) Time $t = 15 \text{ m}\cdot\text{s}^{-1}$. (c) Time $t = 20 \text{ m}\cdot\text{s}^{-1}$.

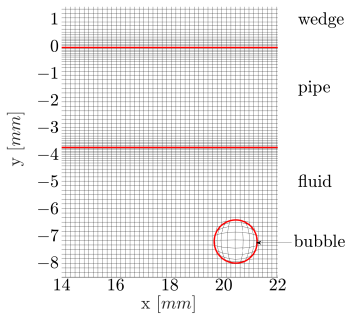


Fig. 13. Nonuniform mesh snapshot.

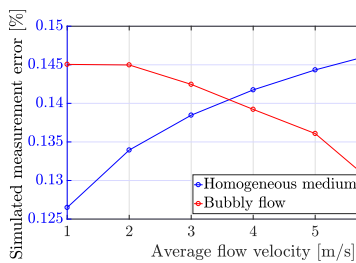


Fig. 14. Comparison of clamp-on flowmeter simulated measurement error for homogeneous medium and bubbly flow.

2.4-GHz base frequency. Final time $t_{\text{final}} = 55 \mu\text{s}$ of one simulation is reached in 27.7 h after 27550 iterations.

The simulated measurement error as a function of various background flow velocities \bar{v}_{0x} is presented in Fig. 11. For the homogeneous flow, the model yields more than

99.6% accuracy, which is due to the fact that the exact value of the hydraulic factor k_h is used in the flow equation (35) and because spectral methods for problems with smooth parameters exhibit exceptional accuracy. An example of received signals is depicted in Fig. 12(a) showing two identical wave packets shifted by Δt . The error for the multiphase flow is not only several orders higher, but it also exhibits high deviation. This is because of the correlation approach that is used to obtain Δt from the simulated received signals, which is very sensitive to the shape of the signal's envelope. As the bubble cluster moves between the upstream and downstream measurements, the reciprocity of the system is violated, which

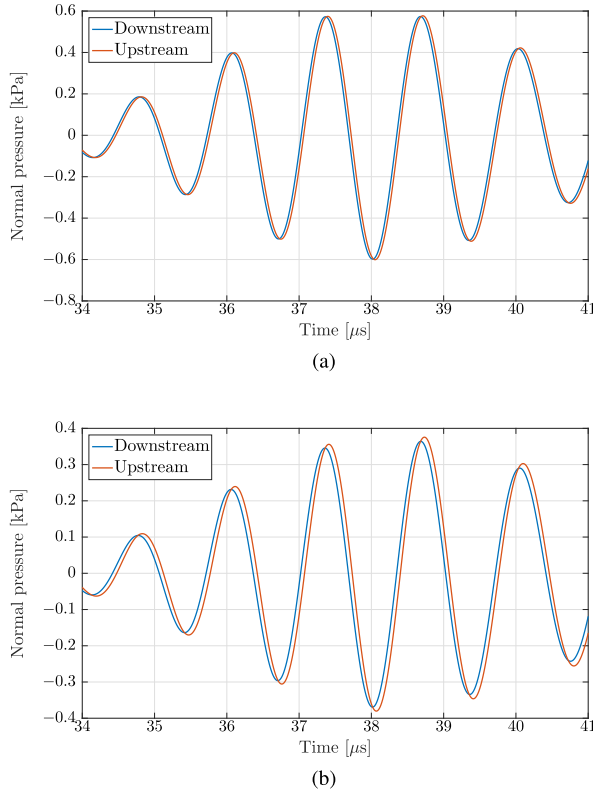


Fig. 16. Comparison of the simulated received signals for homogeneous and multiphase flow for clamp-on TTUF, $v_{0x} = 5 \text{ m.s}^{-1}$. (a) Homogeneous flow. (b) Multiphase flow.

results in two qualitatively different signals, as shown in Fig. 12(b).

B. Clamp-On Ultrasonic Flowmeter

A Clamp-on ultrasonic flowmeter is simulated as a system of layers, which is schematically depicted in Fig. 9. All simulation parameters are tabulated in Table VI. This time, both mesh adaptation techniques were implemented. A mesh was locally refined in the regions of the material interfaces, and grid points in the vicinity of the bubble cluster were subsequently redistributed to describe the inclusion's geometry more accurately. An example of such a discretized physical domain is presented in Fig. 13.

The simulated measurement errors are presented in Fig. 14. For homogeneous medium, the error is again small. On the other hand, the clamp-on flowmeter accuracy appears to be more robust in case of the multiphase flow compared with the in-line configuration. This is due to the fact that the frequency of the input signal f_c is chosen, such that a resonance of the shear wave in the pipe wall is achieved for the given ϑ_w and material properties [32]. By doing so, the acoustic beam then radiates and is also received over much wider apertures, which can be seen from the simulation snapshots in Fig. 15. This partially compensates for the presence of high contrast scatterers. Fig. 16(b) depicts the received signals for the same measurement conditions as in Fig. 12(b) for the in-line flowmeter. The signals' envelopes have a similar shape this time and are therefore more correlated.

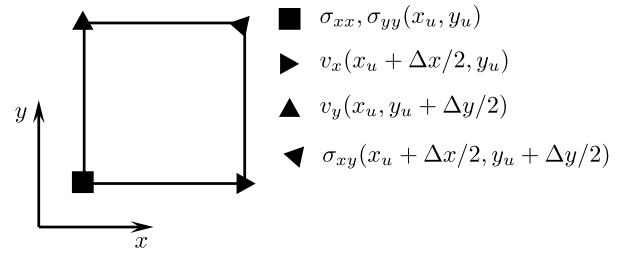


Fig. 17. 2-D staggered grid scheme.

VII. CONCLUSION

A goal of this paper was to extend the standard PSTD method by mesh adaptation techniques, such that propagation in both in-line and clamp-on TTUFs can be described more accurately. The method was validated against analytical solutions showing clear benefit when using nonuniform meshes when simulating reflection and transmission from elastic plates and reflections from high contrast agents, e.g., air bubbles in water.

The model was then used to demonstrate the effect of the multiphase flow on the measurement accuracy when assumption of the homogeneous flow is used. The clamp-on flowmeter results confirmed how exciting resonance in the pipe wall can partially compensate for scattering from the second phase.

APPENDIX

Numerical implementation of (4) and (5) becomes rather complex after introducing PMLs and grid mapping. Therefore, an example of the full development for an arbitrary variable is presented here to avoid any confusion. The equations in the Appendix represent fully developed v_x on nonuniform staggered grids for the pseudospectral Fourier collocation method. The development is presented in 2-D only with $v_{0y} = 0$ and $f_i = 0$, which gives a clear indication of the method. The extension to 3-D is, however, quite straightforward. It is assumed that the background flow is only a weak function of time and its gradients, e.g., $(\partial v_{0x}/\partial x_n)$, are precalculated and stored so they need not be obtained at each time integration stage. The staggered grid scheme employed in this work is schematically depicted in Fig. 17. Field variables need to be sometimes evaluated at grid points other than those predefined by the staggered scheme. This is done by using the trigonometric interpolation following the same framework, as described in Section III-A. For example, $\sigma_{xy}(x_u^+, y_u)$ is interpolated by

$$\sigma_{xy}(x_u^+, y_u) \approx \text{Re}(\mathcal{F}^{-1}(e^{-ik\Delta x/2}\mathcal{F}(\sigma_{xy}(x_u^+, y_u^+)))) \quad (40)$$

Velocity field v_x is calculated at each time step as

$$\begin{aligned} k_{1x}v_x(x_n^+, y_n, t) &= e^{G_x(x_n^+, y_n)\Delta t} \\ &\times \left(\frac{1}{\rho(x_n^+, y_n)} \frac{\partial \sigma_{xx}(x_n, y_n, t)}{\partial x_n^+} \right. \\ &\quad - v_{0x}(x_n^+, y_n) \frac{\partial v_x(x_n^+, y_n, t)}{\partial x_n} \\ &\quad \left. - v_x(x_n^+, y_n, t) \frac{\partial v_{0x}(x_n^+, y_n)}{\partial x_n} \right) \end{aligned}$$

$$\begin{aligned}
& \frac{\partial \sigma_{xx}(x_n, y_n, t)}{\partial x_n^+} \\
&= \frac{dx_u}{dx_n}(x_n^+, y_n) \cdot \frac{\partial \sigma_{xx}(x_u, y_u, t)}{\partial x_u^+} \\
&+ \frac{dy_u}{dx_n}(x_n^+, y_n) \cdot \frac{\partial \sigma_{xx}(x_u^+, y_u, t)}{\partial y_u} \\
&+ \frac{\Delta t}{2} \cdot \frac{\partial k_{1y} \sigma_{xx}(x_u^+, y_u, t + \Delta t/2)}{\partial y_u} \\
& \frac{\partial v_x(x_n^+, y_n, t)}{\partial x_n} \\
&= \frac{dx_u}{dx_n}(x_n^+, y_n) \cdot \frac{\partial v_x(x_u^+, y_u, t)}{\partial x_u} \\
&+ \frac{dy_u}{dx_n}(x_n^+, y_n) \cdot \frac{\partial v_x(x_u^+, y_u, t)}{\partial y_u} \\
&+ \frac{\Delta t}{2} \cdot \frac{\partial k_{1x} v_x(x_u^+, y_u, t + \Delta t/2)}{\partial x_u} \\
&+ \frac{\Delta t}{2} \cdot \frac{\partial k_{1y} v_x(x_u^+, y_u, t + \Delta t/2)}{\partial x_u} \\
& k_{1y} v_x(x_n^+, y_n, t) \\
&= e^{G_y(x_n^+, y_n) \Delta t} \\
&\times \left(\frac{1}{\rho(x_n^+, y_n)} \frac{\partial \sigma_{xy}(x_n^+, y_n^+, t)}{\partial y_n^-} \right. \\
&\quad \left. - \frac{\partial v_{0x}(x_n^+, y_n)}{\partial y_n} v_y(x_n^+, y_n, t) \right) \\
& \frac{\partial \sigma_{xy}(x_n^+, y_n^+, t)}{\partial y_n^-} \\
&= \frac{dx_u}{dy_n}(x_n^+, y_n) \cdot \frac{\partial \sigma_{xy}(x_u^+, y_u, t)}{\partial x_u} \\
&+ \frac{dy_u}{dy_n}(x_n^+, y_n) \cdot \frac{\partial \sigma_{xy}(x_u^+, y_u^+, t)}{\partial y_u^-} \\
& k_{2x} v_x(x_n^+, y_n, t + \Delta t/2) \\
&= e^{G_x(x_n^+, y_n) \Delta t/2} \\
&\times \left(\frac{1}{\rho(x_n^+, y_n)} \frac{\partial \sigma_{xx}(x_n, y_n, t + \Delta t/2)}{\partial x_n^+} \right. \\
&\quad - v_{0x}(x_n^+, y_n) \frac{\partial v_x(x_n^+, y_n, t + \Delta t/2)}{\partial x_n} \\
&\quad \left. - v_x(x_n^+, y_n, t + \Delta t/2) \frac{\partial v_{0x}(x_n^+, y_n)}{\partial x_n} \right) \\
& \frac{\partial \sigma_{xx}(x_n, y_n, t + \Delta t/2)}{\partial x_n^+} \\
&= \frac{dx_u}{dx_n}(x_n^+, y_n) \\
&\times \left(\frac{\partial \sigma_{xx}(x_u, y_u, t)}{\partial x_u^+} \right. \\
&\quad + \frac{\Delta t}{2} \cdot \frac{\partial k_{1x} \sigma_{xx}(x_u, y_u, t + \Delta t/2)}{\partial x_u^+} \\
&\quad + \frac{\Delta t}{2} \cdot \frac{\partial k_{1y} \sigma_{xx}(x_u, y_u, t + \Delta t/2)}{\partial x_u^+} \left. \right) \\
&+ \frac{dy_u}{dx_n}(x_n^+, y_n) \\
&\times \left(\frac{\partial \sigma_{xx}(x_u^+, y_u, t)}{\partial y_u} \right. \\
&\quad + \frac{\Delta t}{2} \cdot \frac{\partial k_{1x} \sigma_{xx}(x_u^+, y_u, t + \Delta t/2)}{\partial y_u} \left. \right) \\
& \frac{\partial v_x(x_n^+, y_n, t + \Delta t/2)}{\partial x_n} \\
&= \frac{dx_u}{dx_n}(x_n^+, y_n) \\
&\times \left(\frac{\partial v_x(x_u^+, y_u, t + \Delta t/2)}{\partial x_u} \right. \\
&\quad + \frac{\Delta t}{2} \cdot \frac{\partial k_{1x} v_x(x_u^+, y_u, t + \Delta t/2)}{\partial x_u} \\
&\quad + \frac{\Delta t}{2} \cdot \frac{\partial k_{1y} v_x(x_u^+, y_u, t + \Delta t/2)}{\partial x_u} \left. \right) \\
&+ \frac{dy_u}{dx_n}(x_n^+, y_n) \\
&\times \left(\frac{\partial v_x(x_u^+, y_u, t)}{\partial y_u} \right. \\
&\quad + \frac{\Delta t}{2} \cdot \frac{\partial k_{1x} v_x(x_u^+, y_u, t + \Delta t/2)}{\partial y_u} \\
&\quad + \frac{\Delta t}{2} \cdot \frac{\partial k_{1y} v_x(x_u^+, y_u, t + \Delta t/2)}{\partial y_u} \left. \right) \\
& k_{2y} v_x(x_n^+, y_n, t + \Delta t/2) \\
&= e^{G_y(x_n^+, y_n) \Delta t/2} \\
&\times \left(\frac{1}{\rho(x_n^+, y_n)} \frac{\partial \sigma_{xy}(x_n^+, y_n^+, t + \Delta t/2)}{\partial y_n^-} \right. \\
&\quad \left. - \frac{\partial v_{0x}(x_n^+, y_n)}{\partial y_n} v_y(x_n^+, y_n, t + \Delta t/2) \right) \\
& \frac{\partial \sigma_{xy}(x_n^+, y_n^+, t + \Delta t/2)}{\partial x_n^+} \\
&= \frac{dx_u}{dy_n}(x_n^+, y_n) \\
&\times \left(\frac{\partial \sigma_{xy}(x_u^+, y_u, t + \Delta t/2)}{\partial x_u} \right. \\
&\quad + \frac{\Delta t}{2} \cdot \frac{\partial k_{1x} \sigma_{xy}(x_u^+, y_u, t + \Delta t/2)}{\partial x_u} \\
&\quad + \frac{\Delta t}{2} \cdot \frac{\partial k_{1y} \sigma_{xy}(x_u^+, y_u, t + \Delta t/2)}{\partial x_u} \left. \right) \\
&+ \frac{dy_u}{dy_n}(x_n^+, y_n) \\
&\times \left(\frac{\partial \sigma_{xy}(x_u^+, y_u^+, t + \Delta t/2)}{\partial y_u^-} \right. \\
&\quad + \frac{\Delta t}{2} \cdot \frac{\partial k_{1x} \sigma_{xy}(x_u^+, y_u^+, t + \Delta t/2)}{\partial y_u^-} \\
&\quad + \frac{\Delta t}{2} \cdot \frac{\partial k_{1y} \sigma_{xy}(x_u^+, y_u^+, t + \Delta t/2)}{\partial y_u^-} \left. \right) \\
& k_{3x} v_x(x_n^+, y_n, t + 3/4 \cdot \Delta t)
\end{aligned}$$

$$\begin{aligned}
&= e^{G_x(x_n^+, y_n) \Delta t/4} \\
&\quad \times \left(\frac{1}{\rho(x_n^+, y_n)} \frac{\partial \sigma_{xx}(x_n, y_n, t + 3/4 \cdot \Delta t)}{\partial x_n^+} \right. \\
&\quad \quad - v_{0x}(x_n^+, y_n) \frac{\partial v_x(x_n^+, y_n, t + 3/4 \cdot \Delta t)}{\partial x_n} \\
&\quad \quad \left. - v_x(x_n^+, y_n, t + 3/4 \cdot \Delta t) \frac{\partial v_{0x}(x_n^+, y_n)}{\partial x_n} \right) \\
&\frac{\partial \sigma_{xx}(x_n, y_n, t + 3/4 \cdot \Delta t)}{\partial x_n^+} \\
&= \frac{dx_u}{dx_n}(x_n^+, y_n) \\
&\quad \times \left(\frac{\partial \sigma_{xx}(x_u, y_u, t)}{\partial x_u^+} \right. \\
&\quad \quad + \frac{3\Delta t}{4} \cdot \frac{\partial k_{2x} \sigma_{xx}(x_u, y_u, t + 3/4 \cdot \Delta t)}{\partial x_u^+} \\
&\quad \quad \left. + \frac{3\Delta t}{4} \cdot \frac{\partial k_{2y} \sigma_{xx}(x_u, y_u, t + 3/4 \cdot \Delta t)}{\partial x_u^+} \right) \\
&\quad + \frac{dy_u}{dx_n}(x_n^+, y_n) \\
&\quad \times \left(\frac{\partial \sigma_{xx}(x_u^+, y_u, t)}{\partial y_u} \right. \\
&\quad \quad + \frac{3\Delta t}{4} \cdot \frac{\partial k_{2x} \sigma_{xx}(x_u^+, y_u, t + 3/4 \cdot \Delta t)}{\partial y_u} \\
&\quad \quad \left. + \frac{3\Delta t}{4} \cdot \frac{\partial k_{2y} \sigma_{xx}(x_u^+, y_u, t + 3/4 \cdot \Delta t)}{\partial y_u} \right) \\
&\frac{\partial v_x(x_n^+, y_n, t + 3/4 \cdot \Delta t)}{\partial x_n} \\
&= \frac{dx_u}{dx_n}(x_n^+, y_n) \\
&\quad \times \left(\frac{\partial v_x(x_u^+, y_u, t + 3/4 \cdot \Delta t)}{\partial x_u} \right. \\
&\quad \quad + \frac{3\Delta t}{4} \cdot \frac{\partial k_{2x} v_x(x_u^+, y_u, t + 3/4 \cdot \Delta t)}{\partial x_u} \\
&\quad \quad \left. + \frac{3\Delta t}{4} \cdot \frac{\partial k_{2y} v_x(x_u^+, y_u, t + 3/4 \cdot \Delta t)}{\partial x_u} \right) \\
&\quad + \frac{dy_u}{dx_n}(x_n^+, y_n) \\
&\quad \times \left(\frac{\partial v_x(x_u^+, y_u, t)}{\partial y_u} \right. \\
&\quad \quad + \frac{3\Delta t}{4} \cdot \frac{\partial k_{2x} v_x(x_u^+, y_u, t + 3/4 \cdot \Delta t)}{\partial y_u} \\
&\quad \quad \left. + \frac{3\Delta t}{4} \cdot \frac{\partial k_{1y} v_x(x_u^+, y_u, t + 3/4 \cdot \Delta t)}{\partial y_u} \right) \\
&k_{3y} v_x(x_n^+, y_n, t + 3/4 \cdot \Delta t) \\
&= e^{G_y(x_n^+, y_n) \Delta t/4} \\
&\quad \times \left(\frac{1}{\rho(x_n^+, y_n)} \frac{\partial \sigma_{xy}(x_n^+, y_n^+, t + 3/4 \cdot \Delta t)}{\partial y_n^-} \right. \\
&\quad \quad \left. - \frac{\partial v_{0x}(x_n^+, y_n)}{\partial y_n} v_y(x_n^+, y_n, t + 3/4 \cdot \Delta t) \right)
\end{aligned}$$

$$\begin{aligned}
&\frac{\partial \sigma_{xy}(x_n^+, y_n^+, t + 3/4 \cdot \Delta t)}{\partial x_n^+} \\
&= \frac{dx_u}{dy_n}(x_n^+, y_n) \\
&\quad \times \left(\frac{\partial \sigma_{xy}(x_u^+, y_u, t + 3/4 \cdot \Delta t)}{\partial x_u} \right. \\
&\quad \quad + \frac{3\Delta t}{4} \cdot \frac{\partial k_{2x} \sigma_{xy}(x_u^+, y_u, t + 3/4 \cdot \Delta t)}{\partial x_u} \\
&\quad \quad \left. + \frac{3\Delta t}{4} \cdot \frac{\partial k_{2y} \sigma_{xy}(x_u^+, y_u, t + 3/4 \cdot \Delta t)}{\partial x_u} \right) \\
&\quad + \frac{dy_u}{dy_n}(x_n^+, y_n) \\
&\quad \times \left(\frac{\partial \sigma_{xy}(x_u^+, y_u^+, t + 3/4 \cdot \Delta t)}{\partial y_u^-} \right. \\
&\quad \quad + \frac{3\Delta t}{4} \cdot \frac{\partial k_{2x} \sigma_{xy}(x_u^+, y_u^+, t + 3/4 \cdot \Delta t)}{\partial y_u^-} \\
&\quad \quad \left. + \frac{3\Delta t}{4} \cdot \frac{\partial k_{2y} \sigma_{xy}(x_u^+, y_u^+, t + 3/4 \cdot \Delta t)}{\partial y_u^-} \right) \\
&xv_x(x_+, y, t + \Delta t) \\
&= e^{G_x(x_+, y) \Delta t} v_x(x_+, y, t) \\
&\quad + 2/9 \cdot \Delta t \cdot k_{1x} v_x(x_+, y, t) \\
&\quad + 1/3 \cdot \Delta t \cdot k_{2x} v_x(x_+, y, t + \Delta t/2) \\
&\quad + 4/9 \cdot \Delta t \cdot k_{3x} v_x(x_+, y, t + 3/4 \cdot \Delta t) \\
&yv_x(x_+, y, t + \Delta t) \\
&= e^{G_y(x_+, y) \Delta t} v_x(x_+, y, t) \\
&\quad + 2/9 \cdot \Delta t \cdot k_{1y} v_x(x_+, y, t) \\
&\quad + 1/3 \cdot \Delta t \cdot k_{2y} v_x(x_+, y, t + \Delta t/2) \\
&\quad + 4/9 \cdot \Delta t \cdot k_{3y} v_x(x_+, y, t + 3/4 \cdot \Delta t) \\
&v_x(x_+, y, t + \Delta t) \\
&= xv_x(x_+, y, t + \Delta t) \\
&\quad + yv_x(x_+, y, t + \Delta t)
\end{aligned}$$

ACKNOWLEDGMENT

The authors would like to acknowledge support from the *Innovation Fund Denmark* and from the *DeIC National HPC Center* for access to computational resources on *Abacus 2.0*. They would also like to thank A.-A. Popa for his help with the experimental measurements.

REFERENCES

- [1] L. C. Lynnworth and Y. Liu, "Ultrasonic flowmeters: Half-century progress report, 1955–2005," *Ultrasonics*, vol. 44, pp. e1371–e1378, Dec. 2006. [Online]. Available: <http://www.sciencedirect.com/science/article/pii/S0041624X06000849>
- [2] B. Funck and A. Mitzkus, "Acoustic transfer function of the clamp-on flowmeter," *IEEE Trans. Ultrason., Ferroelect., Freq. Control*, vol. 43, no. 4, pp. 569–575, Jul. 1996.
- [3] D. V. Mahadeva, R. C. Baker, and J. Woodhouse, "Studies of the accuracy of clamp-on transit time ultrasonic flowmeters," in *Proc. IEEE Instrum. Meas. Technol. Conf. (IMTC)*, May 2008, pp. 969–973.
- [4] D. V. Mahadeva, R. C. Baker, and J. Woodhouse, "Further studies of the accuracy of clamp-on transit-time ultrasonic flowmeters for liquids," *IEEE Trans. Instrum. Meas.*, vol. 58, no. 5, pp. 1602–1609, May 2009.

- [5] M. Kupnik, P. O'Leary, A. Schroder, and I. Rungger, "Numerical simulation of ultrasonic transit-time flowmeter performance in high temperature gas flows," in *Proc. IEEE Symp. Ultrason.*, vol. 2, Oct. 2003, pp. 1354–1359.
- [6] B. Iooss, C. Lhuillier, and H. Jeanneau, "Numerical simulation of transit-time ultrasonic flowmeters: Uncertainties due to flow profile and fluid turbulence," *Ultrasonics*, vol. 40, no. 9, pp. 1009–1015, 2002. [Online]. Available: <http://www.sciencedirect.com/science/article/pii/S0041624X02003876>
- [7] M. Bezdek, H. Landes, A. Rieder, and R. Lerch, "A coupled finite-element, boundary-integral method for simulating ultrasonic flowmeters," *IEEE Trans. Ultrason., Ferroelect., Freq. Control*, vol. 54, no. 3, pp. 636–646, Mar. 2007.
- [8] A. Luca, R. Marchiano, and J. C. Chassaing, "A discontinuous Galerkin approach for the numerical simulation of transit-time ultrasonic flowmeters," in *Proc. IEEE Int. Ultrason. Symp.*, Sep. 2014, pp. 935–938.
- [9] A. Luca, R. Marchiano, and J. C. Chassaing, "Numerical simulation of transit-time ultrasonic flowmeters by a direct approach," *IEEE Trans. Ultrason., Ferroelect., Freq. Control*, vol. 63, no. 6, pp. 886–897, Jun. 2016.
- [10] A. Luca, K. Fodil, and A. Zerarka, "Full-wave numerical simulation of ultrasonic transit-time gas flowmeters," in *Proc. IEEE Int. Ultrason. Symp. (IUS)*, Sep. 2016, pp. 1–4.
- [11] L. N. Trefethen, *Spectral Methods in MATLAB*. Philadelphia, PA, USA: SIAM, 2000.
- [12] B. E. Treeby and B. T. Cox, "k-Wave: MATLAB toolbox for the simulation and reconstruction of photoacoustic wave fields," *J. Biomed. Opt.*, vol. 15, no. 2, pp. 021314-1–021314-12, 2010. [Online]. Available: <http://dx.doi.org/10.1117/1.3360308>
- [13] CyberLogic, Inc. New York, NY, USA. (2016). *Wave 2000 and Wave3000*. [Online]. Available: <http://www.cyberlogic.org>
- [14] COMSOL, Inc. Burlington, VT, USA. (2016). *COMSOL Multiphysics*. [Online]. Available: <https://www.comsol.com>
- [15] ANSYS, Inc. Canonsburg, PA, USA, (2016). *ANSYS*. [Online]. Available: <http://www.ansys.com>
- [16] B. E. Treeby, "Modeling nonlinear wave propagation on nonuniform grids using a mapped k-space pseudospectral method," *IEEE Trans. Ultrason., Ferroelect., Freq. Control*, vol. 60, no. 10, pp. 2208–2213, Oct. 2013.
- [17] C. S. Peskin, *Flow Patterns Around Heart Valves: A Digital Computer Method for Solving the Equations of Motion*. Ann Arbor, MI, USA: UMI, 1973. [Online]. Available: <https://books.google.dk/books?id=6tsnOAAACAAJ>
- [18] R. Mittal and G. Iaccarino, "Immersed boundary methods," *Annu. Rev. Fluid Mech.*, vol. 37, no. 1, pp. 239–261, 2005. [Online]. Available: <https://doi.org/10.1146/annurev.fluid.37.061903.175743>
- [19] M. Simurda, B. Lassen, L. Duggen, and N. T. Basse, "A Fourier collocation approach for transit-time ultrasonic flowmeter under multi-phase flow conditions," *J. Comput. Acoust.*, vol. 25, no. 1, p. 1750005, 2016. [Online]. Available: <http://www.worldscientific.com/doi/abs/10.1142/S0218396X17500059>
- [20] M. Simurda, L. Duggen, B. Lassen, and N. T. Basse, "Modelling of transit-time ultrasonic flow meters under multi-phase flow conditions," in *Proc. IEEE Int. Ultrason. Symp. (IUS)*, Sep. 2016, pp. 1–6.
- [21] B. Auld, *Acoustic Fields and Waves in Solids*. Melbourne, FL, USA: Krieger, 1990. [Online]. Available: <https://books.google.com/books?id=qUGEPwAACAAJ>
- [22] A. D. Pierce, "Wave equation for sound in fluids with unsteady inhomogeneous flow," *J. Acoust. Soc. Amer.*, vol. 87, no. 6, pp. 2292–2299, 1990. [Online]. Available: <http://scitation.aip.org/content/asa/journal/jasa/87/6/10.1121/1.399073>
- [23] L. N. Trefethen, *Spectral Methods in MATLAB*. Philadelphia, PA, USA: SIAM, 2000. [Online]. Available: <http://epubs.siam.org/doi/abs/10.1137/1.9780898719598>
- [24] K. Firouzi, B. T. Cox, B. E. Treeby, and N. Saffari, "A first-order k-space model for elastic wave propagation in heterogeneous media," *J. Acoust. Soc. Amer.*, vol. 132, no. 3, pp. 1271–1283, 2012. [Online]. Available: <http://scitation.aip.org/content/asa/journal/jasa/132/3/10.1121/1.4730897>
- [25] K. Firouzi, A. Nikoozadeh, and B. T. Khuri-Yakub, "Modeling elastic waves in heterogeneous anisotropic media using a k-space method," in *Proc. IEEE Int. Ultrason. Symp.*, Sep. 2014, pp. 1356–1359.
- [26] B. Treeby and B. T. Cox, "A computationally efficient elastic wave model for media with power-law absorption," in *Proc. IEEE Int. Ultrason. Symp. (IUS)*, Jul. 2013, pp. 1037–1040.
- [27] M. Ghrist, B. Fornberg, and T. A. Driscoll, "Staggered time integrators for wave equations," *SIAM J. Numer. Anal.*, vol. 38, no. 3, pp. 718–741, 2000. [Online]. Available: <http://dx.doi.org/10.1137/S0036142999351777>
- [28] K. C. Meza-Fajardo and A. S. Papageorgiou, "A nonconvolutional, split-field, perfectly matched layer for wave propagation in isotropic and anisotropic elastic media: Stability analysis," *Bull. Seismologic. Soc. Amer.*, vol. 98, no. 4, pp. 1811–1836, 2008. [Online]. Available: <http://www.bssaonline.org/content/98/4/1811.abstract>
- [29] M. Tabei, T. D. Mast, and R. C. Waag, "A k-space method for coupled first-order acoustic propagation equations," *J. Acoust. Soc. Amer.*, vol. 111, no. 1, pp. 53–63, 2002. [Online]. Available: <http://scitation.aip.org/content/asa/journal/jasa/111/1/10.1121/1.1421344>
- [30] M. Willatzen, "Ultrasound transducer modeling-received voltage signals and the use of half-wavelength window layers with acoustic coupling layers," *IEEE Trans. Ultrason., Ferroelect., Freq. Control*, vol. 46, no. 5, pp. 1164–1174, Sep. 1999.
- [31] M. Willatzen, "Ultrasound transducer modeling-general theory and applications to ultrasound reciprocal systems," *IEEE Trans. Ultrason., Ferroelect., Freq. Control*, vol. 48, no. 1, pp. 100–112, Jan. 2001.
- [32] M. A. Ainslie, "Plane-wave reflection and transmission coefficients for a three-layered elastic medium," *J. Acoust. Soc. Amer.*, vol. 97, no. 2, pp. 954–961, 1995. [Online]. Available: <http://scitation.aip.org/content/asa/journal/jasa/97/2/10.1121/1.412074>



Matej Simurda received the B.Sc. degree in mechanical engineering from the Brno University of Technology, Brno, Czech Republic, in 2010, and the M.Sc. degree in mechatronics and the Ph.D. degree in applied mathematical modeling from the University of Southern Denmark, Sønderborg, Denmark, in 2013 and 2017, respectively.

He is currently a Numerical Specialist with Orsted, Fredericia, Denmark.



Lars Duggen received the M.Sc. degree in mechatronics engineering and the Ph.D. degree in applied mathematical modeling from the University of Southern Denmark (SDU), Sønderborg, Denmark, in 2008 and 2011, respectively.

He is currently an Associate Professor in mechatronics with SDU.



Nils T. Basse received the B.Sc., M.Sc., and Ph.D. degrees from the Niels Bohr Institute, University of Copenhagen, Copenhagen, Denmark, in 1996, 1998, and 2002, respectively.

He was a Post-Doctoral Associate with the Plasma Science and Fusion Center, Massachusetts Institute of Technology, Cambridge, MA, USA, from 2002 to 2005. From 2006 to 2011, he was a Scientist and a Principal Scientist with ABB Switzerland Ltd., Corporate Research, Baden-Dättwil, Switzerland. From 2011 to 2016, he was a Senior Research Engineer with Siemens A/S, Flow Instruments, Sønderborg, Denmark. He is currently a computation fluid dynamics Expert with Danfoss A/S, Refrigeration and Air Conditioning Controls, Nordborg, Denmark. His present research interests include industrial flow phenomena.



Benny Lassen received the M.Sc. degree in mathematics and the Ph.D. degree in mathematical modeling from the University of Southern Denmark, Sønderborg, Denmark, in 2002 and 2005, respectively.

He was with Lund University, Lund, Sweden, where he was financed by a Villum Kann Rasmussen Postdoctoral stipend for one year. He was an Assistant Professor and an Associate Professor with the University of Southern Denmark from 2007 to 2010 and from 2007 to 2016, respectively. He is currently a Senior Numerical Specialist with Orsted, Denmark.